



OPEN Large-field high-resolution X-ray AKB microscope for measuring hydrodynamic instabilities at the SG-III prototype laser facility

Liang Chen^{1,2}, Pin Yang³, Jie Xu^{1,2}✉, Baozhong Mu^{1,2}, Wenjie Li^{1,2}, Xinye Xu^{1,2}, Mingtao Li^{1,2}, Jinbo Li^{1,2}, Xin Wang^{1,2}, Xing Zhang³, Feng Wang³, Zhanshan Wang^{1,2} & Dong Yang³

X-ray imaging with a large field of view (FOV) and high resolution is extremely important for Rayleigh–Taylor instability measurement with a small amplitude and high spatial frequency in laser inertial confinement fusion. We developed an advanced Kirkpatrick–Baez (AKB) microscope based on the quadratic-aberration theory to realize a large FOV and high resolution. This microscope was assembled and tested in a laboratory, and it was then successfully applied for imaging the hydrodynamic instability of a perturbation target in implosion experiments at the Shenguang-III prototype laser facility. Imaging results demonstrate that the AKB microscope can achieve an optimal resolution of $\sim 0.53 \mu\text{m}$ and $\sim 0.40 \mu\text{m}$ and a spatial resolution of $< 1.5 \mu\text{m}$ within a $300\text{-}\mu\text{m}$ FOV and $< 4.5 \mu\text{m}$ in a 1-mm FOV.

Keywords X-ray imaging, Rayleigh–Taylor instability, High-resolution, AKB microscope

The indirect-drive approach to inertial confinement fusion (ICF) is to achieve ignition through the spherical compression of a deuterium–tritium (DT)-filled capsule driven by X-rays generated from the laser irradiation of a high-Z hohlraum^{1,2}. In laser ICF experiments, hydrodynamic instability of the inner interface of the pellet during the implosion deceleration stage seriously affects the compression density and intensifies hot spot mixing, considering reducing the overall implosion performance^{3–9}. ICF diagnostic systems are required to study the involvement of the Rayleigh–Taylor (R–T) instability in mixing and the transition to turbulence in the high-energy density regime. To effectively diagnose the growth of microstructures due to hydrodynamic instability, the diagnostic system must realize a high spatial resolution of $< 3 \mu\text{m}$ in a 1-mm FOV^{10–13}.

Several methods have been developed for high-resolution diagnosis of hydrodynamic instability in laser ICF. The Crystal Backlighter Imager (CBI) is a spherically-bent crystal imager at the National Ignition Facility (NIF) with a resolution limit of $7 \mu\text{m}$ ^{14,15}. However, further improvement of the resolution requires using a toroidal crystal, and the near-normal incidence requires an overly large diagnostic stereo angle, which will occupy the diagnostic optical path of other devices. A Fresnel zone plate (FZP)^{16–19} design has been calibrated at the NIF with a 9 keV zinc (Zn) backlighter, demonstrating a resolution of $2.3 \pm 0.4 \mu\text{m}^2$. However, FZPs have severe chromatic aberration, and their high spatial resolution depends on the monochromaticity of the light source, so they have limited application to ICF and are more commonly used in synchrotron radiation.

Kirkpatrick–Baez (KB) microscopes are diagnostic devices based on grazing incidence reflection that can achieve a high resolution of $4\text{--}6 \mu\text{m}$ for a central field of view (FOV) of $200\text{--}300 \mu\text{m}$ ^{20,21}. The optimal resolution of a KB microscope is limited by spherical aberration, and the high-resolution FOV is limited by off-axis aberration. The KBA configuration can effectively correct the off-axis aberration and expand the FOV by adding a spherical mirror with the same curvature in each of the two-dimensional directions²². The quadratic surface effectively eliminates spherical aberration at points on the axis, a spatial resolution of $< 2 \mu\text{m}$ has been achieved in the central FOV in the laboratory²³. The advanced KB (AKB) configuration proposed by Kodama et al. achieved a spatial resolution of better than $3 \mu\text{m}$ in an FOV of 800 mm ²⁴. The AKB configuration comprises two pairs of hyperbolic and elliptical cylindrical mirrors, which satisfies the Abbe sine condition for high spatial

¹MOE Key Laboratory of Advanced Micro-Structured Materials, School of Physics Science and Engineering, Tongji University, 1239 Siping Road, Shanghai 200092, China. ²School of Physics Science and Engineering, Tongji University, Shanghai 200092, China. ³Laser Fusion Research Center, China Academy of Engineering Physics, Mianyang 621900, China. ✉email: 1310581@tongji.edu.cn

resolution. However, this study used the 25–75% criterion for resolution calibration while subsequent studies on the AKB configuration focused on synchrotron radiation^{25,26}.

In this study, we developed an AKB configuration based on the quadratic-aberration theory to realize an X-ray microscope with a large FOV and resolution of <1 μm at the central FOV. The large FOV is realized by using a metal monolayer with a large angle bandwidth, and the initial positions of two quadratic surfaces are located by machining two ultra-smooth reflecting surfaces on a mirror base. To evaluate the performance, offline X-ray imaging and resolution calibration experiments were performed in the laboratory, and grid resolution and hydrodynamic instability tests were conducted at the Shenguang III (SG-III) prototype laser facility.

System design Optical design

The AKB configuration focuses separately in the meridional and tangential directions with two reflections in a given direction. Figure 1 shows a schematic of the AKB microscope in one-dimensional, which is based on hyperbolic and elliptical mirrors. The object point is located at the right focus F_3 of the hyperbolic surface. The rays emitted by the object point first pass through the hyperbolic surface to form a virtual image at the common focus F_2 of the hyperbolic and elliptical surfaces. The actual rays are reflected by the hyperbolic surface, and they finally converge at the right focus F_1 of the elliptical surface to form a real image. Because the two surfaces are quadratic, the central object point F_3 satisfies the Fermat principle, so the ideal image ultimately appears there.

Suppose that the angle between the incident main ray F_3M_1 and optical axis is θ_3 and that the angles between the main ray and optical axis after one and two reflections are θ_2 and θ_1 , respectively. Then, M_1 and M_2 are the central positions of the two mirrors, the first and second theoretical angles of incidence are θ_{10} and θ_{20} , and the magnification of the system is M . Based on geometric optics and conics properties, the following can be deduced using the law of reflection:

$$\begin{cases} \theta_1 = \frac{2(\theta_{10} + \theta_{20})}{1+M} \\ \theta_2 = \frac{2(M\theta_{10} - \theta_{20})}{1+M} \\ \theta_3 = \frac{2M(\theta_{10} + \theta_{20})}{1+M} \end{cases} \quad (1)$$

Equation (1) can be employed to determine the angles between the main ray and optical axis. For one hyperbola, these are easily obtained from the law of reflection and the geometric relations of triangles:

$$\begin{cases} a_1 = \frac{u_{10}}{2} (M_h - 1) \\ b_1 = \frac{u_{10}}{2} \sqrt{M_h^2 - (2\cos 2\theta_{10} + 1) M_h + 2} \end{cases} \quad (2)$$

where u_{10} is the object distance, M_h is the magnification of the hyperbolic mirror, a_1 is the semi-real axis of the hyperbola, and b_1 is the semi-imaginary axis of the hyperbola. The same method can be used to calculate the parameters of an elliptical surface:

$$\begin{cases} u_{20} = d + M_h u_{10} \\ a_2 = \frac{u_{20}}{2} (M_e + 1) \\ b_2 = \frac{u_{20}}{2} \sqrt{2(1 - \cos 2\theta_{20})} M_e \\ M = M_e M_h \end{cases} \quad (3)$$

where u_{20} is the object distance of the elliptical mirror, M_e is the magnification of the elliptical mirror, M is the magnification of the optical system, a_2 is the semi-major axis of the ellipse, and b_2 is the semi-minor axis of the

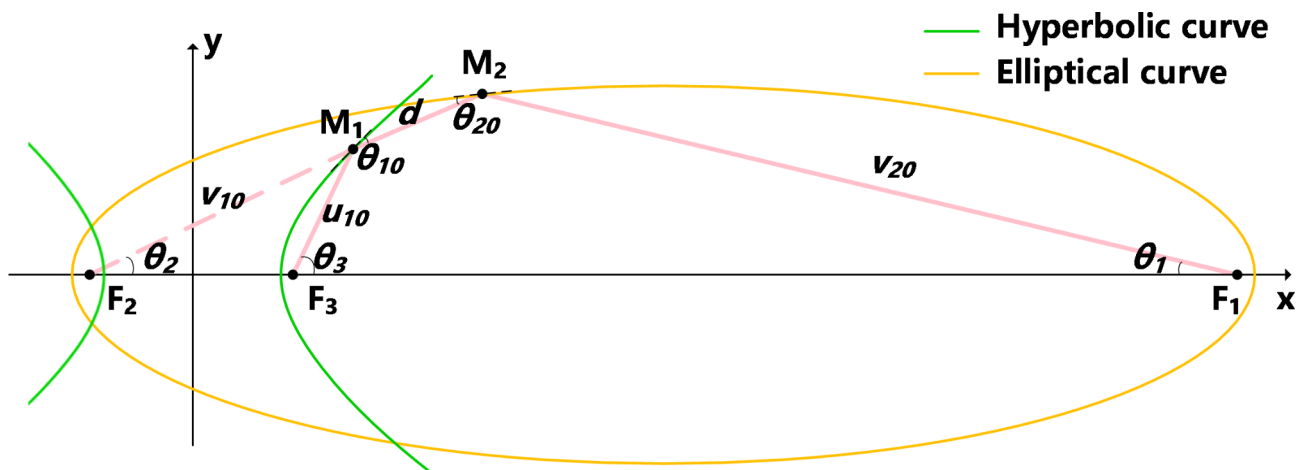


Fig. 1. Schematic of the AKB microscope.

ellipse. With the above equations, if we are given the object distance u_{10} , magnification M , and grazing incident angle θ_{10} and θ_{20} , then the initial structural parameters of the hyperbolic and elliptical mirrors can be obtained. Because one-dimensional direction mirrors can only achieve one-dimensional focusing, the meridional and sagittal directions need to be calculated independently.

For the conventional KB configuration, the mirror length acts as an aperture diaphragm, and the grazing incidence angle bandwidth acts as a FOV diaphragm. However, for the AKB configuration of the two-mirror structure, the distance between the two reflecting surfaces separates the FOV diaphragm from the aperture diaphragm. As shown in Fig. 2a, the schematic diagram of the optical path over a certain range of central FOV is given as FOV_{cen} . The hyperbolic mirror predominates in limiting the range of the rays passing through the system and acts as the aperture diaphragm. Elliptical mirror acts as FOV diaphragm and determines the FOV angle σ of the system. For marginal FOV, the role of the apertures and FOV diaphragms of the two mirrors becomes complicated. In order to analyze the effective FOV of the system we need to solve for the variation of the geometric solid angle with the FOV by using the ray-tracing procedure.

The angular bandwidth of an optical system is determined by the superimposed effects of aperture and FOV. As shown in Fig. 2b, considering the edge rays reflection at full aperture and full FOV of the system. The angle between the two mirrors is κ . The positive and negative FOV edge rays are reflected from the hyperbolic edge and incident on the edge of the elliptical mirror. At this point the grazing incidence angle of the elliptical mirror ranges from θ_{2min} to θ_{2max} . Thus, the geometric angular bandwidth of the system is $\Delta\theta_2$. The following expression can be given based on the geometric relationship:

$$\begin{cases} u_{10}\theta_{10} + q = \left(u_{10} - \frac{d_1}{2}\right) * (\kappa - \theta_{2min}) \\ u_{10}\theta_{10} - q = \left(u_{10} + \frac{d_1}{2}\right) * (\kappa - \theta_{2max}) \\ \Delta\theta_2 = \theta_{2max} - \theta_{2min} \end{cases} \quad (4)$$

where q is the half-FOV and d_1 is the hyperbolic mirror length. The geometric angular bandwidth in the FOV of $2q$ can be estimated by the above method, and the angular bandwidth of the film coated on the mirror surface needs to be matched with $\Delta\theta_2$.

To facilitate X-ray plasma diagnosis of high-power laser equipment, the working energy point of the microscope was set to 8.0 keV (corresponding to the Cu Ka1 line) to ensure a large observation depth. To

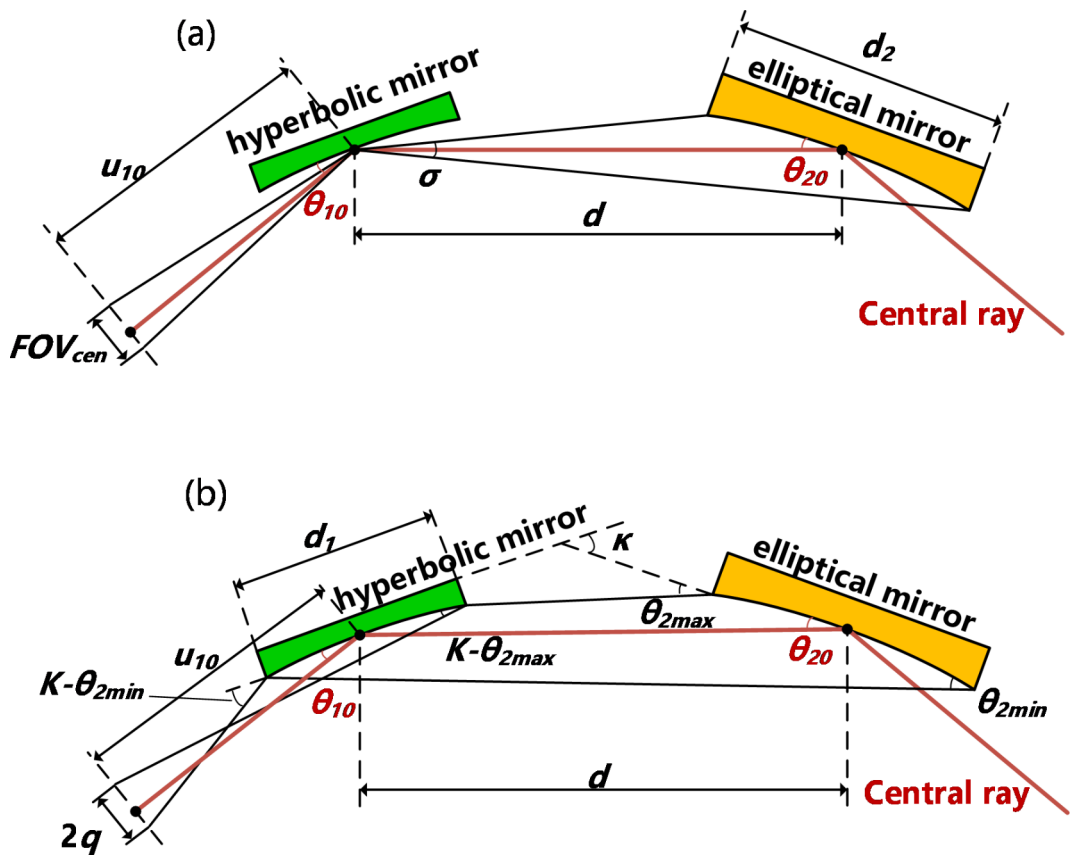


Fig. 2. Schematic of the FOV diaphragm and angular bandwidth of an AKB microscope. (a) Optical path diagram of the elliptical mirror as a FOV diaphragm, (b) schematic diagram of the angular bandwidth optical path of AKB microscope.

Direction	Sagittal	Meridian
Grazing angle(°)	0.45	0.45
Object distance(mm)	200	235
Magnification	25	21.3
θ_3 (°)	1.7398	1.7268
System length(mm)	5460	5460
Quadratic equation	Hyperbolic	$\frac{x^2}{a_1^2} - \frac{y^2}{b_1^2} = 1$
	Elliptical	$\frac{(x-2730)^2}{a_2^2} + \frac{y^2}{b_2^2} = 1$
Quadratic parameter(mm)	Hyperbolic	$a_1 = 108.3255$ $b_1 = 2.2674$
	Elliptical	$a_2 = 2838.3741$ $b_2 = 11.8806$
		$a_1 = 129.0761$ $b_1 = 2.6740$ $a_2 = 2859.1327$ $b_2 = 12.8363$

Table 1. Parameters of the AKB Microscope.

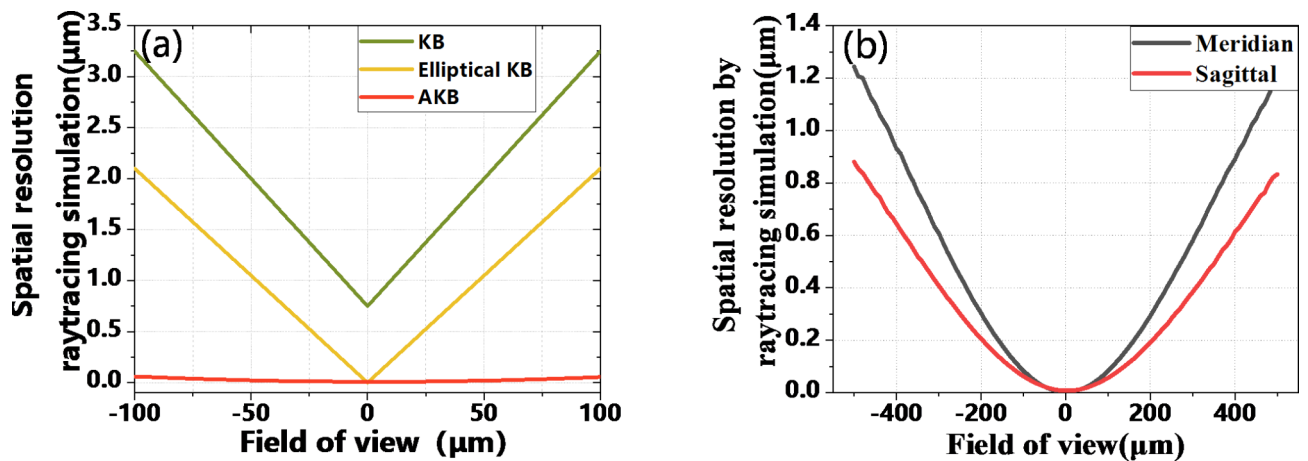


Fig. 3. Resolution curves of KB configuration, elliptical KB configuration and AKB configuration. (a) The resolution simulations of KB configuration, elliptical KB configuration and AKB configuration, (b) resolution of the AKB configuration in two-dimensional direction.

consider the influence of the detector pixel size on the spatial resolution, the magnification of the microscope was designed at 20.0 to 25.0 times. Based on the experimental conditions of the laser facility and the requirements for diagnosis hydrodynamic instability, we set the initial parameters of the microscope to an object distance of 200 mm and central incident angle of 0.45° for the hyperbolic and elliptical mirrors. Specifically, the hyperbolic magnification M_h is 2 times in both the sagittal and meridional directions, and the elliptical magnification M_e is 12.5 and 10.65 times, respectively. These parameters were employed to calculate a geometric solid angle of 1.2×10^{-7} sr. Table 1 presents further details on the optical parameters.

Simulation

We have compiled ray-tracing program for the AKB microscope, and we can simulate the optical performance of the system under full-FOV conditions. For the same object distance of 200 mm, grazing incidence angle of 0.45° and magnification of 25, the resolution curves of KB configuration, elliptical KB configuration and AKB configuration are shown in Fig. 3a. Due to the limitations of spherical and off-axis aberrations, KB microscopes are unable to achieve high resolution in the full-FOV. The ellipsoidal KB guarantees high resolution in the central FOV, but the high-resolution area is small. A simulation of the resolution of the AKB microscope in the two-dimensional direction is shown in Fig. 3b. It can be seen that a resolution better than $1.3 \mu\text{m}$ can be achieved in 1-mm FOV. As a result of the greater magnification, the resolution in meridional direction will be better than in sagittal direction.

For the AKB microscope, we adopted a Pt monolayer design with flat response characteristics, and each working surface has a grazing incident angle of 0.45° . The reflectivity-angle curve can be obtained in ray-tracing simulations. The corresponding distribution can be obtained based on the film structure and solid angle for geometric light collection. As shown in Fig. 4a, the reflective efficiency of the AKB microscope was symmetric in the meridian and sagittal directions with a peak reflectance of 39% at the center of the FOV and reflectance of 28% at the edge of the FOV. The incident angle and actual object distance corresponding to different positions in the object FOV are slightly different from the theoretical calculation, so the geometric solid angle for light

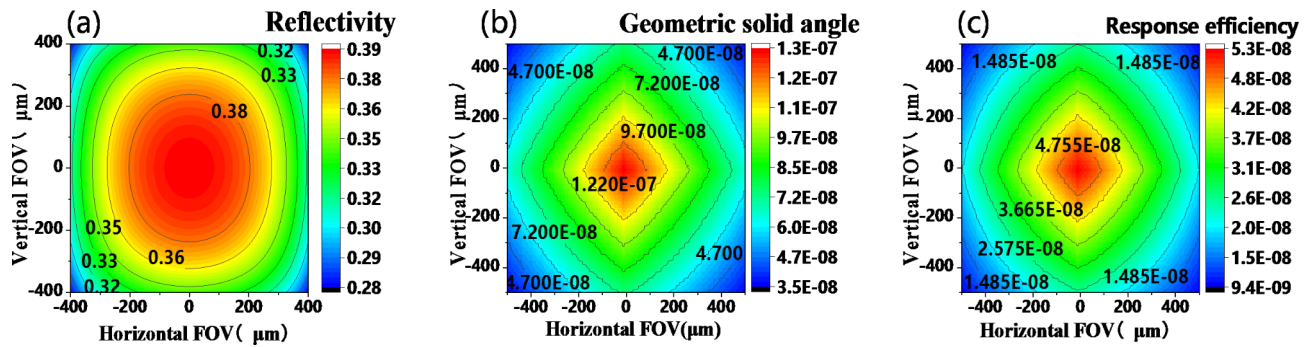


Fig. 4. Reflective strength of the AKB microscope in ray-tracing simulations. (a) efficiency, (b) geometric solid angle, and (c) response efficiency of the AKB microscope.

collection of the full-FOV should be calculated to determine the overall response efficiency. Because part of the rays at the edge of the FOV fail to enter the elliptical mirror after being reflected by the hyperbolic mirror, this causes a loss of the solid angle for light collection. Thus, we need to normalize the amount of ray passing through. The light collection capacities can be calculated in two dimensions and multiplied to obtain the geometric solid angle, as shown in Fig. 4b. For a FOV of $\pm 500 \mu\text{m}$, the geometric solid angle varies from 3.3×10^{-8} to 1.2×10^{-7} sr, and the response distribution of the microscope can be obtained by multiplying the reflectivity distribution of the system, as shown in Fig. 4c. The peak response efficiency of the AKB microscope was obtained at 4.7×10^{-8} sr. The angular bandwidth of the system is 0.28° in meridional direction and 0.26° in sagittal direction, which can have a reflectivity of 70% in a 600- μm FOV and a reflectivity of 31% in a 1-mm FOV.

Results and methods

Laboratory resolution testing

Figure 5 shows the experimental arrangement of the AKB microscope in the X-ray imaging laboratory. The high-precision electronic control displacement table has an adjustment accuracy of $10 \mu\text{m}$. The reflector substrate was made of Si, and the effective area of the hyperbolic and elliptical surfaces was $2 \times 10 \text{ mm}$. Through surface characterization with a phase-shift interference microscope, the average values of the shape error, slope error, and roughness were determined to be 0.694 nm , $0.158 \mu\text{rad}$, and 0.179 nm , respectively. The non-central working area of the mirror was in contact with a pair of high-precision prisms with tightly controlled dimensions and inclination that were fixed by rear reclining. The prisms provided the initial spatial attitude of the mirrors to guarantee that the vector height of the working area of the mirror matched the theoretically calculated value from the conic curve. The parallelism between the optical axis of the microscope and the axis of the experimental platform was judged by a position sensor. The six-axis precision electronic control adjustment frame was used to carry the microscope and adjust the two axes to coincide with a pitch and roll alignment accuracy of $\sim 0.5 \mu\text{rad}$. The center of the image point on the image surface was always near the optical axis, and the position of the charge-coupled device (CCD) or framing camera was easily determined by laser indication.

The target material of the X-ray backlight was a Cu anode with $\text{K}\alpha 1$ characteristic line emission at 8.0 keV . The focal spot size of the backlight was $1 \times 1 \text{ mm}^2$. A gold grid with a diameter of 2 mm and a marked center was placed on the object, and the number of periods varied from 150 to 2000 mesh grids. A mixed mesh grid was used to mark the center of the FOV, and high-mesh grids were used to test the spatial resolution of the system. Meshes were replaced under the supervision of two high-precision CCDs from different directions, and the replacement accuracy was $< 5 \mu\text{m}$, which corresponded to half the line width of the mesh. A Hard X-ray scintillation detector was used as the image recording equipment with a pixel size of $4.54 \mu\text{m}$ and maximum acquisition area for a single image of $12.5 \text{ mm} \times 10 \text{ mm}$. A 5-m-long helium tube with a concentration of more than 90% was placed in the optical path to reduce X-ray attenuation and improve the air environment and signal-to-noise ratio.

Resolution calibration

Figure 6 shows X-ray grid backlight images and the results of the laboratory test to determine the resolution of the AKB microscope. The spatial resolution was calibrated by using 10–90% of the grid shadow edge²⁷. The 1000-mesh Au grid shown in Fig. 6a was imaged at 40 kV by using a 30-mA continuous X-ray source with an exposure time of 20 min . The grid period was $\sim 25 \mu\text{m}$, the grid width was $\sim 6 \mu\text{m}$, and the thickness was $\sim 20 \mu\text{m}$. The initial position of the grid was set to $(0, 0)$, which was centered on the marked point. The grid was moved to the positions of $(+250, 0)$, $(+250, +250)$, $(0, +250)$, $(-250, +250)$, $(-250, 0)$, $(-250, -250)$, $(0, -250)$, and $(-250, -250)$ to obtain mesh imaging results for a FOV of 1 mm . For each move to a different set of coordinates, the X-ray backlight and CCD needed to be moved proportionally and simultaneously to ensure that the edges of the grid were also illuminated. Figure 6a shows the imaging result of the 1000-mesh Au grid within a FOV of $\pm 500 \mu\text{m}$ comprising nine pictures. The red circle is the positioning center of the image stitching, $75 \mu\text{m}$ away from the center of the FOV. A clear and sharp grid line can be observed at the central FOV that gradually blurred toward the edge, and a good resolution was maintained throughout the FOV. These results showed that a spatial resolution of $< 4.5 \mu\text{m}$ could be achieved even at the edge of the FOV.

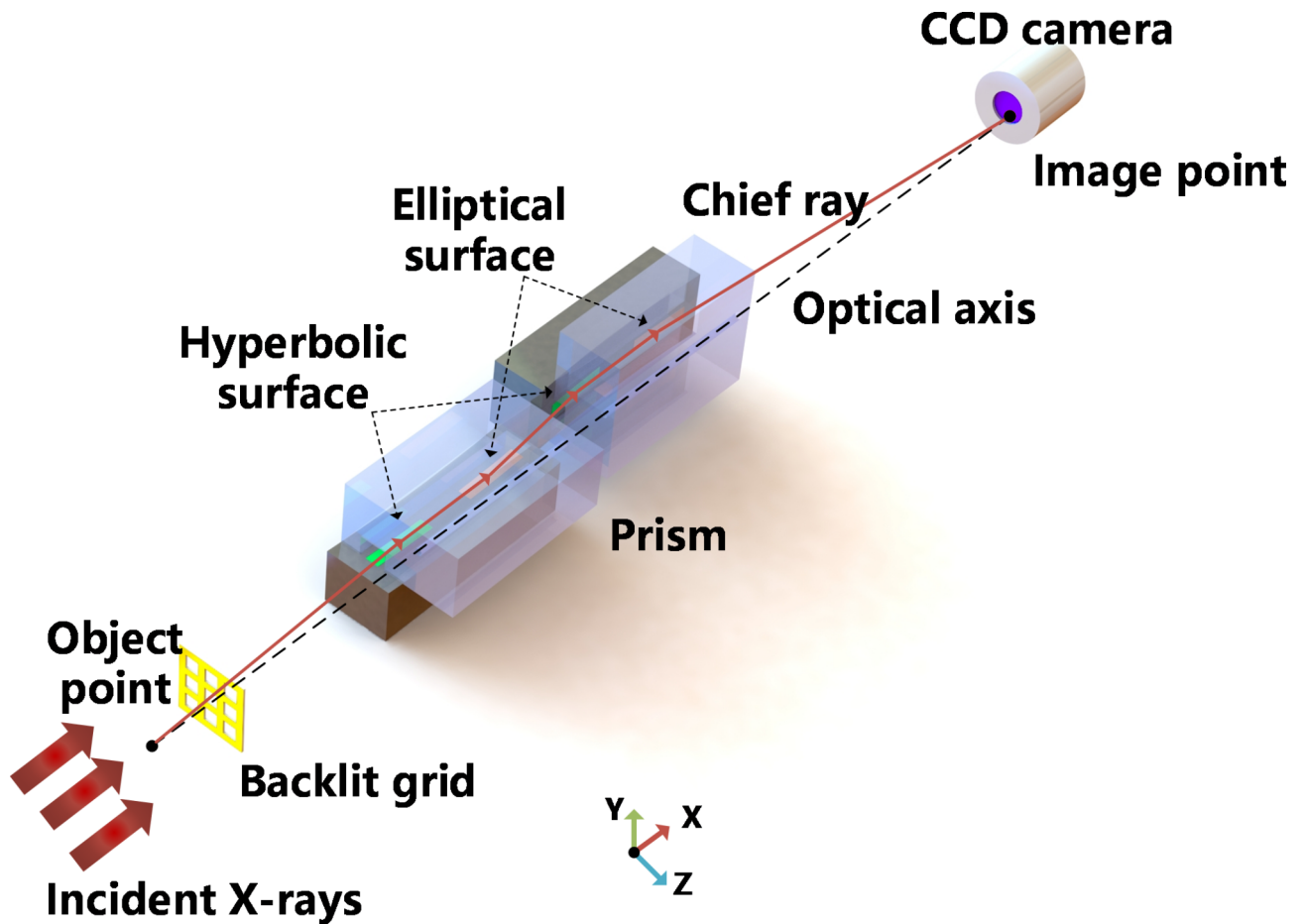


Fig. 5. Experimental arrangement of the AKB microscope.

The high spatial resolution of the microscope can be characterized by using a high mesh grid. Figure 6b shows the backlit imaging results of a 1000-mesh grid and intensity profiles in the central 200- μm FOV in the two-dimensional direction. Figure 6c,d show the measurements of black and red lines used to obtain the spatial resolution of the entire FOV in two directions. Specifically, we perform rectangular integration on the single direction intensity profiles and then use Boltzmann function fitting to obtain the edge response. A polynomial fit was performed to estimate the resolution curve. The optimal spatial resolution of the AKB microscope reached ~ 0.53 and ~ 0.40 μm in the meridional and sagittal directions, respectively. The resolution was better in the sagittal direction than in the meridional direction due to greater magnification, which is consistent with the trend of the simulation curves. The AKB microscope had a spatial resolution of < 1.5 μm in a 300- μm FOV and < 4.5 μm in a 1-mm FOV. Compared with conventional KB diagnostic equipment, the AKB microscope has a much larger high-resolution area.

Online experimental arrangement

The AKB microscope was applied in the X-ray radiography of the R-T instabilities growth on the SG-III prototype laser facility. Two types of targets were used: an Au mesh, and an R-T perturbation target. First, grid backlighting experiments were performed on the facility with the aim of testing the static resolving power of the microscope and locating the recording equipment which is a scintillation detector. The imaging grid was employed with a position sensor to locate the center of the chamber. A diaphragm hole was placed in front of the diagnostic module to effectively shield stray light from outside the FOV while a 100- μm -thick Kapton layer and 200- μm -thick polycarbonate layer were installed to shield against debris. Further, by adjusting the laser parameters and replacing the target, the study of the R-T instabilities can be conducted.

In the experiments, the V backlighter was driven by four laser beams from the chamber bottom, and other four laser beams directly drive the planar CH-Al target with the preset perturbations on the Al surface. The pulse width of the backlighter and driving laser are 0.5 ns and 1 ns. Each laser beam is a square pulse with 800 J of energy. The experimental optical path layout is shown in Fig. 7, the driving laser is injected from the top. The R-T perturbation target mainly includes two CH ablator layers, the perturbation samples and the CH foam. The target is wrapped in an Al shielding case. The diagnostic direction of the microscope is perpendicular to the perturbation growth plane, and the center of the FOV can be calculated from the shock wave velocity.

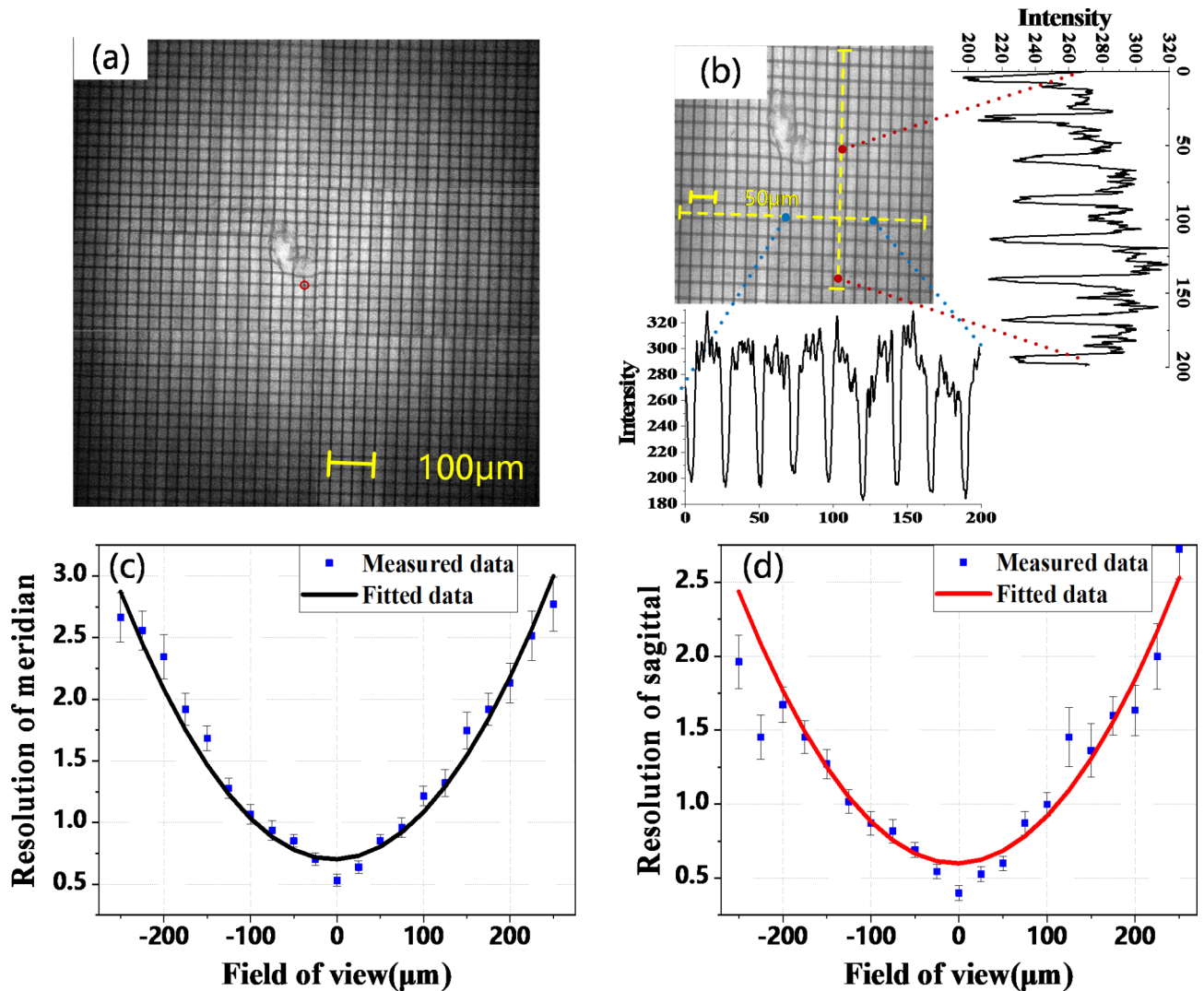


Fig. 6. Grid imaging results of the AKB microscope in laboratory tests. (a) 1000-mesh grid imaging of a 1-mm FOV; (b) 1000-mesh grid imaging of the central FOV; Spatial resolutions of the FOV in the (c) meridional and (d) sagittal directions measured using the 10–90% criterion.

Imaging results at the SG-III prototype

The time integral images of the Au mesh and the R-T instability were recorded with a pixel size of 13.5 μm. Figure 8a shows the 1000-mesh Au grid imaging results with the V backlight, and Fig. 8b shows the obtained spatial resolution. The backlight impingement point was slightly off-center with a resolution of up to 1 μm for the central FOV and a resolution of < 3 μm for a ±250 μm FOV. The resolution at the edge of the FOV was slightly reduced compared to the laboratory results. Figure 8c shows the imaging results for the R-T sinusoidal perturbation target with the V backlight and the spikes and protrusions of the perturbed interface can be observed. For the reduction of resolution at the laser facility, we believe the reason for this is that a shock wave with a velocity of 40 km/s produces a temporal blur of about 20 μm for 0.5-ns backlight time, and this effect can be effectively reduced by using the framing camera. Using a 10-ps time-resolved framing camera can reduce temporal blur to less than 1 μm under current conditions. However, effective diagnosis of hydrodynamic fine structure also requires backlight imaging with a certain contrast. It is not the case that the shorter the gating time the better the resolution, this needs to be considered in conjunction with the following factors. The specific value of the temporal blur that can be reduced needs to be combined with hydrodynamic model simulations, plasma backlighting efficiency, mirror reflection efficiency, and quantum efficiency of the recording device.

Conclusion

We developed an AKB microscope that is suitable for diagnosing hydrodynamic instability in ICF research. The large FOV and high resolution of < 1 μm at the central FOV are effective for diagnosing the fine structure of cusps and bubbles during ICF implosions. Moreover, the AKB microscope has a wide energy spectrum of ~8.0 keV. Laboratory results showed that the AKB microscope could achieve an optimal resolution of ~0.53 and ~0.40 μm in the meridional and sagittal directions, respectively, and spatial resolutions of < 1.5 μm within

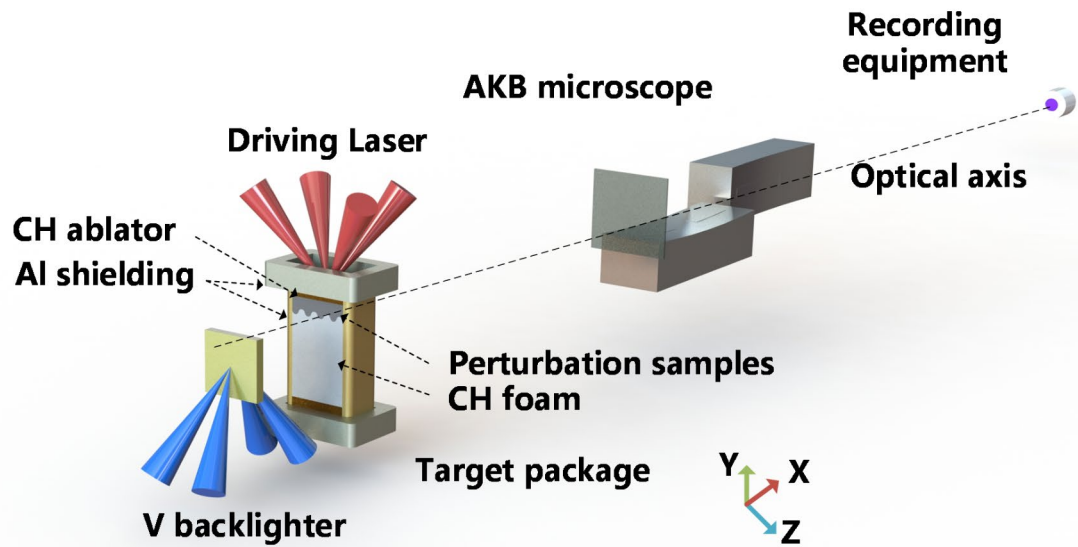


Fig. 7. Online experimental arrangement of the laser facility.

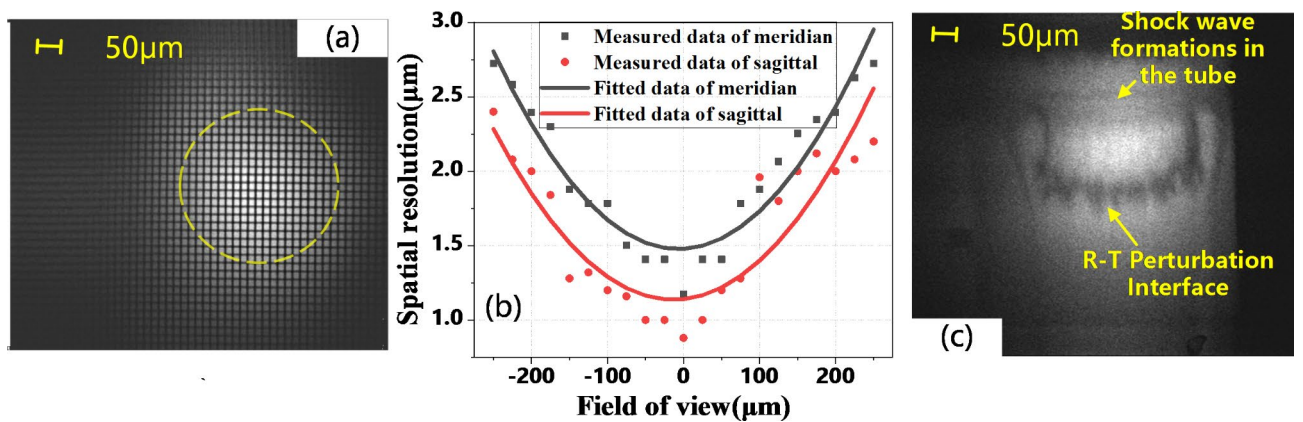


Fig. 8. Imaging results of the laser facility with the AKB microscope. (a) 1000-mesh grid imaging of the central FOV, (b) spatial resolution using the 10–90% criterion, and (c) imaging results for an R–T sinusoidal perturbation target with V backlight.

a 300- μm FOV and $< 4.5 \mu\text{m}$ in a 1-mm FOV. The microscope was used in studying R–T instabilities in a planar geometry at the SG-III prototype laser facility and successfully observing the hydrodynamic instability of a sinusoidal perturbation target during implosion.

Data availability

Data underlying the results presented in this paper are not publicly available at this time but may be obtained from the corresponding author upon reasonable request.

Received: 20 July 2024; Accepted: 5 November 2024

Published online: 16 November 2024

References

- Nuckolls, J., Wood, L., Thiessen, A. & Zimmerman, G. Laser compression of matter to super-high densities: Thermonuclear (CTR) applications. *Nature* **239**, 139–142. <https://doi.org/10.1038/239139a0> (1972).
- Lindl, J. D. et al. The physics basis for ignition using indirect-drive targets on the national ignition facility. *Phys. Plasmas* **11**, 339–491. <https://doi.org/10.1063/1.1578638> (2004).
- Lindl, J. D. *Inertial Confinement Fusion* (Springer, 1998).
- Hurricane, O. et al. Inertially confined fusion plasmas dominated by alpha-particle self-heating. *Nat. Phys.* **12**, 800–806. <https://doi.org/10.1038/nphys3720> (2016).
- Ma, T. et al. The role of hot spot mix in the low-foot and high-foot implosions on the NIF. *Phys. Plasma* **24**, 056311. <https://doi.org/10.1063/1.4983625> (2017).
- Cheng, B. et al. Effects of asymmetry and hot-spot shape on ignition capsules. *Phys. Rev. E* **98**, 023203. <https://doi.org/10.1103/PhysRevE.98.023203> (2018).
- Smalyuk, V. A. et al. Review of hydro-instability experiments with alternate capsule supports in indirect-drive implosions on the National Ignition Facility. *Phys. Plasmas* **25**, 072705. <https://doi.org/10.1063/1.5042081> (2018).
- McGlinchey, K. et al. Diagnostic signatures of performance degrading perturbations in inertial confinement fusion implosions. *Phys. Plasmas* **25**, 122705. <https://doi.org/10.1063/1.5064504> (2018).
- Haines, B. M. et al. Robustness to hydrodynamic instabilities in indirectly driven layered capsule implosions. *Phys. Plasmas* **26**, 012707 (2019). <https://doi.org/10.1063/1.5080262>
- Smalyuk, V. A. et al. Review of hydrodynamic instability experiments in inertially confined fusion implosions on National Ignition Facility. *Plasma Phys. Control. Fusion* **62**, 014007 (2020). <https://doi.org/10.1088/1361-6587/ab49f4>
- Town, R. P. J. et al. Dynamic symmetry of indirectly driven inertial confinement fusion capsules on the National Ignition Facility. *Phys. Plasmas* **21**, 056313. <https://doi.org/10.1063/1.4876609> (2014).
- Smalyuk, V. A. et al. Hydrodynamic instability growth of three-dimensional, native-roughness modulations in x-ray driven, spherical implosions at the National Ignition Facility. *Phys. Plasmas* **22**, 072704. <https://doi.org/10.1063/1.4926591> (2015).
- Do, A. et al. High spatial resolution and contrast radiography of hydrodynamic instabilities at the National Ignition Facility. *Phys. Plasmas* **29**, 080703 (2022). <https://doi.org/10.1063/5.0087214>
- Hall, G. N. et al. The Crystal Backlighter Imager: a spherically-bent crystal imager for radiography on the National Ignition Facility. *59th Annual Meeting of the APS Division of Plasma Physics American Physical Society* **90**, 013702 (2019).
- Angulo, A. M. et al. Design of a high-resolution Rayleigh–Taylor experiment with the crystal backlighter imager on the National Ignition Facility. *J. Inst.* **17**, P02025. <https://doi.org/10.48550/arXiv.2112.00085> (2022).
- Mohacsi, I. et al. Interlaced zone plate optics for hard X-ray imaging in the 10 nm range. *Sci. Rep.* **7**, 43624. <https://doi.org/10.1038/srep43624> (2017).
- David, C. et al. Nanofocusing of hard X-ray free electron laser pulses using diamond-based Fresnel zone plates. *Sci. Rep.* **1**, 57. <https://doi.org/10.1038/srep00057> (2011).
- Suzuki, Y. et al. Fabrication and performance test of Fresnel zone plate with 35 nm outermost zone width in hard X-ray region. *X-Ray Opt. Instrum.*, 824387. <https://doi.org/10.1155/2010/824387> (2010).
- Do, A. et al. X-ray imaging of Rayleigh–Taylor instabilities using Fresnel zone plate at the National Ignition Facility. *Rev. Sci. Instrum.* **92**, 053511. <https://doi.org/10.1063/5.0043682> (2021).
- Pickworth, L. A. et al. Visualizing deceleration-phase instabilities in inertial confinement fusion implosions using an enhanced self-emission technique at the National Ignition Facility. *Phys. Plasmas* **25**, 054502. <https://doi.org/10.1063/1.5025188> (2018).
- Xu, J. et al. Development of a flat-field-response, four-channel x-ray imaging instrument for hotspot asymmetry studies. *Rev. Sci. Instrum.* **93**, 103545. <https://doi.org/10.1063/5.0106990> (2022).
- Denetiere, D., Audebert, P., Bahr, R., Bole, S. & Troussel, P. High resolution imaging systems for inertial confinement fusion experiments. *Target. Diagn. Phys. Eng. Inert. Confinement Fusion* **8505**, 85050G. <https://doi.org/10.1117/12.929490> (2012).
- Xu, X. et al. High-resolution elliptical Kirkpatrick–Baez microscope for implosion higher-mode instability diagnosis. *Opt. Express*. **30**, 26761–26773. <https://doi.org/10.1364/OE.463502> (2022).
- Kodama, R. et al. Development of an advanced Kirkpatrick–Baez Microscope. *Opt. Lett.* **21**, 1321–1323. <https://doi.org/10.1364/OE.21.001321> (1996).
- Matsuyama, S. et al. 50-nm-resolution full-field X-ray microscope without chromatic aberration using total-reflection imaging mirrors. *Sci. Rep.* **7**, 46358. <https://doi.org/10.1038/srep46358> (2017).
- Matsuyama, S. et al. Hard-X-ray imaging optics based on four aspherical mirrors with 50 nm resolution. *Opt. Express*. **20**, 10310–10319. <https://doi.org/10.1364/OE.20.010310> (2012).
- Jiang, C. et al. Four-channel toroidal crystal X-ray imager for laser-produced plasmas. *Opt. Express*. **29**, 6133–6146. <https://doi.org/10.1364/OE.415537> (2021).

Acknowledgements

The authors acknowledge the support of the staff at the Laser Fusion Research Center. This work was supported by National Key R&D Program of China (2023YFA1608400), National Natural Science Foundation of China (12075220) and Foundation of Science and Technology on Near-Surface Detection Laboratory (6142414220607).

Author contributions

L.C. mainly completed the manuscript and participated in all works. X.X. established the theoretical modelling and ray-tracing simulations. W.L. and M.L. built the experimental optical path and completed the laboratory resolution tests. J.L. and P.Y. assisted with the imaging experiments on the laser facility. J.X., X.W., and B.M. assisted with the writing and revising of the manuscript. X.Z., F.W., Z.W., and D.Y. were responsible for funds

applications. All authors contributed to the manuscript.

Declarations

Competing interests

The authors declare no competing interests.

Additional information

Correspondence and requests for materials should be addressed to J.X.

Reprints and permissions information is available at www.nature.com/reprints.

Publisher's note Springer Nature remains neutral with regard to jurisdictional claims in published maps and institutional affiliations.

Open Access This article is licensed under a Creative Commons Attribution-NonCommercial-NoDerivatives 4.0 International License, which permits any non-commercial use, sharing, distribution and reproduction in any medium or format, as long as you give appropriate credit to the original author(s) and the source, provide a link to the Creative Commons licence, and indicate if you modified the licensed material. You do not have permission under this licence to share adapted material derived from this article or parts of it. The images or other third party material in this article are included in the article's Creative Commons licence, unless indicated otherwise in a credit line to the material. If material is not included in the article's Creative Commons licence and your intended use is not permitted by statutory regulation or exceeds the permitted use, you will need to obtain permission directly from the copyright holder. To view a copy of this licence, visit <http://creativecommons.org/licenses/by-nc-nd/4.0/>.

© The Author(s) 2024